iScience

CellPress
OPEN ACCESS

Article

# 3D-printed scaffold harboring copper ions combined with near-infrared irradiation for local therapy of cancer

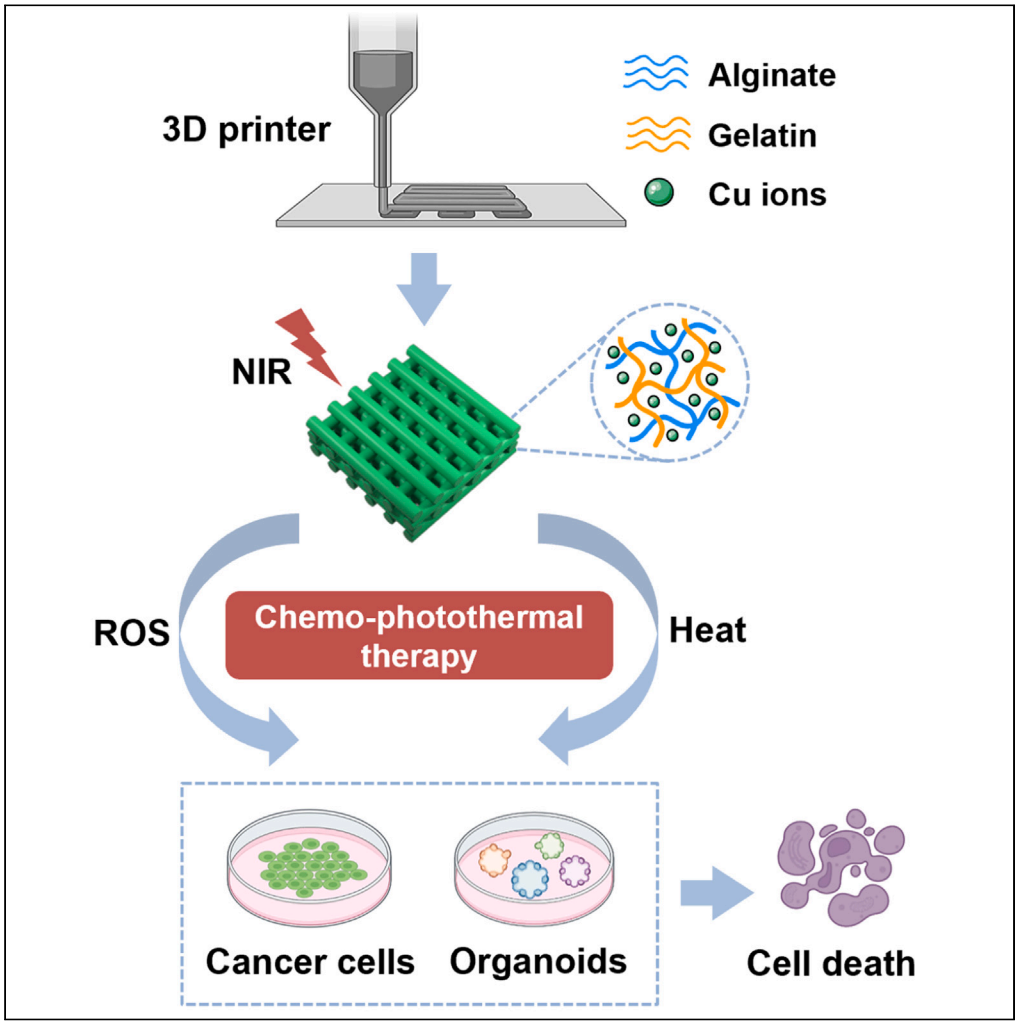


Hao Wei, Dong Chen, Bin Han, ..., Haibo Chen, Yongxiang Luo, Yongsheng Zhao

yourchenhb@163.com (H.C.)
luoyongxiang@szu.edu.cn (Y.L.)
zhaoys69@126.com (Y.Z.)

## Highlights

3D printing a copper-loaded scaffold for local cancer therapy under NIR irradiation

Establishment and characterization of thyroid cancer organoids

The scaffold exhibits a chemo-photothermal therapeutic effect on thyroid cancer

Wei et al., iScience 26, 108076
October 20, 2023 
https://doi.org/10.1016/j.isci.2023.108076

iScience

CellPress
OPEN ACCESS

Article

# 3D-printed scaffold harboring copper ions combined with near-infrared irradiation for local therapy of cancer

Hao Wei,[1,3,4] Dong Chen,[2,4] Bin Han,[2] Peng Li,[2] Hao Jia,[2] Lizhang Zhu,[2] Hao Yang,[1] Deren Lan,[1] Wei Wei,[2] Haibo Chen,[1,*] Yongxiang Luo,[3,*] and Yongsheng Zhao[1,5,*]

## SUMMARY

**Cancer is a major health threat and a leading cause of human death worldwide. Surgical resection is the primary treatment for most cancers; however, some patients develop locoregional recurrence. Here, we developed an *in situ* cancer therapeutic system aimed to locally treat cancer and prevent postoperative recurrence. A functional scaffold, based on alginate/gelatin and crosslinked with copper ions, was fabricated by 3D printing and showed an excellent photothermal effect under near-infrared (NIR) irradiation. The combination of copper ions and NIR effectively killed thyroid cancer cells and patient-derived organoids, indicating a synergetic and broad-spectrum antitumor effect on thyroid cancer through the chemo-photothermal therapy. This implantable stent is designed to provide effective treatment in the vicinity of the tumor site and can be degraded without secondary surgery. The copper-loaded hydrogel scaffold may be a potential candidate for local cancer treatment and pave the way for precise and effective cancer therapy.**

## INTRODUCTION

Cancer is one of the main causes of human death worldwide, and its incidence is increasing year by year. Surgical resection, which aims to remove tumor tissue directly, is the main treatment option for cancer patients. However, local tumor recurrence resulting from minimal or occult residual tumors remains a serious clinical problem. Postoperative adjuvant therapies, such as targeted therapy and systemic chemotherapy, can improve the removal of residual tumor cells and prevent their recurrence and metastasis. Yet, these treatments still face problems of severe toxicity and non-specific distribution to normal cells and tissues. Thus, developing new treatment strategies to overcome these limitations has become a hot topic in cancer research.

In recent years, some novel and effective strategies for cancer treatment have received great attention. As a non-invasive and spatiotemporal controlled treatment technology, photothermal therapy (PTT) has gained a significant role in clinical practice. Upon irradiation with near-infrared (NIR) laser, the heat generated from the absorbed optical energy by photothermal agents can destroy cancer cells through hyperthermia.[1] PTT can reduce tumor burden through local thermal ablation, rendering it a powerful tool for cancer treatment.[2] By locally irradiating with NIR, the hyperthermia (>42°C) generated by photothermal agents can induce apoptosis or necrosis of tumor cells by inhibiting DNA synthesis, damaging cytoskeleton, and destroying cell membrane.[3,4] Chemodynamic therapy (CDT), which converts overexpressed endogenous hydrogen peroxide ($H_2O_2$) to strong oxidized hydroxyl radicals by catalyzing metal ion-mediated Fenton or Fenton-like reactions, plays a role in tumor therapy.[5,6] In CDT, the level of reactive oxygen species (ROS) generation plays an important role in evaluating treatment efficacy. Copper ions-based materials, which function as photosensitizers or Fenton-reaction catalysts, are capable of generating ROS. The generation of ROS can further contribute to the elimination of cancer cells. Moreover, PTT can improve several ROS-related therapy strategies such as photodynamic therapy (PDT) and CDT in different ways.[7] Therefore, integrating $Cu^{2+}$-based PTT and ROS-related therapy into a single platform appears to be an ideal strategy for synergistic cancer treatment. Copper ions have been extensively studied for their photothermal and chemodynamic effects in cancer therapy.[8–13] The traditional method primarily carries metal ions based on nanomaterials. However, the uncertain structure of nanomaterials may result in uncontrolled catalytic effects on Fenton or Fenton-like reaction systems and still cannot change the status quo of systemic delivery.[14]

[1]Department of Nuclear Medicine, Peking University Shenzhen Hospital, Shenzhen 518036, China
[2]Department of Thyroid and Breast Surgery, Peking University Shenzhen Hospital, Shenzhen 518036, China
[3]Guangdong Key Laboratory for Biomedical Measurements and Ultrasound Imaging, Department of Biomedical Engineering, Shenzhen University Medical School, Shenzhen University, Shenzhen 518055, China
[4]These authors contributed equally
[5]Lead contact
*Correspondence: yourchenhb@163.com (H.C.), luoyongxiang@szu.edu.cn (Y.L.), zhaoys69@126.com (Y.Z.)
https://doi.org/10.1016/j.isci.2023.108076

Relevant studies have developed various delivery systems for therapeutic methods, such as hydrogels, polymer scaffolds, polymer micelles, hydrogel/polymer micelle composites, and stimulation-responsive materials.[15] However, these vectors have certain shortcomings as they need to be injected into the body to reach the lesions; especially they are rapidly cleared in the blood circulation and then excessively accumulate in non-target tissues.[16] Local delivery using a 3D-printed stent is an effective method to treat local tumor residue and recurrence, compared to injecting drugs into the systemic circulation. This method minimizes drug distribution throughout the body thereby reducing side effects. Therefore, local delivery using a 3D-printed stent will be a promising way for cancer patients with residual disease and local recurrence.

In this paper, we propose a simple strategy, an implant called Cu/AG scaffold, for cancer treatment. It is based on alginate/gelatin (AG) and crosslinked with cupric chloride ($CuCl_2$). The localized release of copper ions ensures the efficacy of CDT at the lesions, while the photothermal effect of copper ions further reduces the use of copper ions and minimizes potential side effects. We validated the therapeutic effect of the scaffold on six thyroid cancer cell lines and conducted further experiments using six patient-derived organoid cultures derived from clinical tumor specimens. These results demonstrated that the method has a broad-spectrum therapeutic effect in the treatment of thyroid cancer. This proof-of-concept study presents a promising way to develop functional stents for the treatment of residual tumors and prevent postoperative recurrence of cancer.

## RESULTS AND DISCUSSION

### Fabrication and characterization of Cu/AG scaffolds

As the most widely used bioink in 3D bioprinting, alginate was chosen as the main material for the stent due to its excellent biocompatibility and the obvious advantages of easy gelatinization using divalent cationic crosslinking under mild conditions.[17] Gelatin was added for its properties of good biocompatibility and printability, as well as thermosensitive sol-gel transition.[18,19] In our previous studies, we reported a range of concentrated bioinks using alginate and gelatin.[20–22] These concentrated bioinks showed good printability, enhanced mechanical characteristics, and robust structural stability. The printing ink based on alginate undergoes a transition from sol to gel through crosslinking by copper ions (Figure S1). By crosslinking with $CuCl_2$, the scaffold introduces copper ions into the alginate matrix, allowing it with both chemodynamic and photothermal effects against tumors. The amount of copper ions carried by the stent can be controlled by adjusting the concentration of the crosslinking agent to achieve an accurate therapeutic effect. This 3D-printed scaffold can be surgically implanted into the human body; its structure and size can be customized by computer-aided design to perfectly match the surgically induced tissue defects. Due to the degradability of the materials used, surgical removal is not required after treatment, and the material can be degraded by itself.

Here, the Cu/AG scaffolds with different concentrations of copper ions were fabricated through an extrusion-based 3D printing technology by crosslinking with different concentrations of $CuCl_2$ (0, 0.07, 0.1, 0.13, and 0.16 mol/L), denoted as 0-Cu/AG, 0.07-Cu/AG, 0.1-Cu/AG, 0.13-Cu/AG, and 0.16-Cu/AG, respectively. Optical images showed that the color of the resultant scaffolds became darker with the increase of the incorporated copper ions (Figure 1A). The scaffolds exhibited smooth surfaces and uniform structures as observed by scanning electron microscope (SEM) (Figure S2). Energy-dispersive X-ray spectroscopy (EDS) element mapping analysis showed that these elements were evenly distributed in the scaffold (Figure 1B), confirming the successful encapsulation of $Cu^{2+}$. Atomic percentage analysis revealed an increased percentage of copper atoms on the surface of the scaffold with the increasing of the concentration of crosslinking agent (Figure 1C). The measurement of mechanical properties and Young's modulus indicate that the stiffness of the Cu/AG scaffolds is dependent on the concentration of $Cu^{2+}$ in the crosslinking agent (Figures 1D and 1E). The release of $Cu^{2+}$ lasted for about 4 days, and the release rate gradually slowed down compared to the initial burst release (Figure 1F). The Cu/AG scaffolds with a high concentration of crosslinking agent exhibited much higher ionic release (Figure 1F). The *in vitro* degradation of the Cu/AG scaffolds was examined by incubating them in PBS (pH = 7.4, 37°C). As the crosslinking density of $Cu^{2+}$ increased, the degradation rate of the AG scaffold decreased (Figure 1G). Moreover, the degradation profile of the 0.13-Cu/AG scaffolds was simulated in both the normal physiological environment (pH 7.4) and the tumor microenvironment (pH 6.5). There was no significant impact on the degradation of the scaffolds in pH 6.5 and pH 7.4 in the first 5 days. After 5 days, the scaffolds in both the pH 6.5 and pH 7.4 environments exhibited accelerated degradation, which was noticeably different from the degradation rate in a neutral environment (Figure 1H).

Furthermore, we assessed the *in vitro* photothermal performance of the 3D-printed Cu/AG scaffolds. The 808 nm NIR light was chosen for the photothermal application with the Cu/AG scaffold due to its highest absorption rate in the UV-vis-NIR absorption spectra (Figure S3). Under NIR laser irradiation (1.3 W/cm$^2$) for 2.5 min, a significant temperature rise in Cu/AG scaffolds was observed with a dependence on the $Cu^{2+}$ concentration (Figure 1I). By comparison, the temperature of the AG scaffold only increased by ~8.5°C under the same irradiation conditions. The photothermal effects of the Cu/AG scaffolds were dependent on the laser power density. As the laser power increased, the temperature of the Cu/AG scaffolds also elevated (Figures 1J and S4). Additionally, no significant temperature decrease was found even under five cycles of laser irradiation (Figures 1K and S5).

Copper ions, as a photothermal agent in PTT, have the important characteristic of photothermal conversion. Therefore, the photothermal conversion efficiency of Cu/AG scaffold was evaluated. The photothermal conversion efficiency ($\eta$) of the 0.13-Cu/AG scaffold can be calculated according to the following equation:

$$\eta = \frac{hA\Delta T_{max} - Qs}{I\left(1 - 10^{-A\lambda}\right)}$$

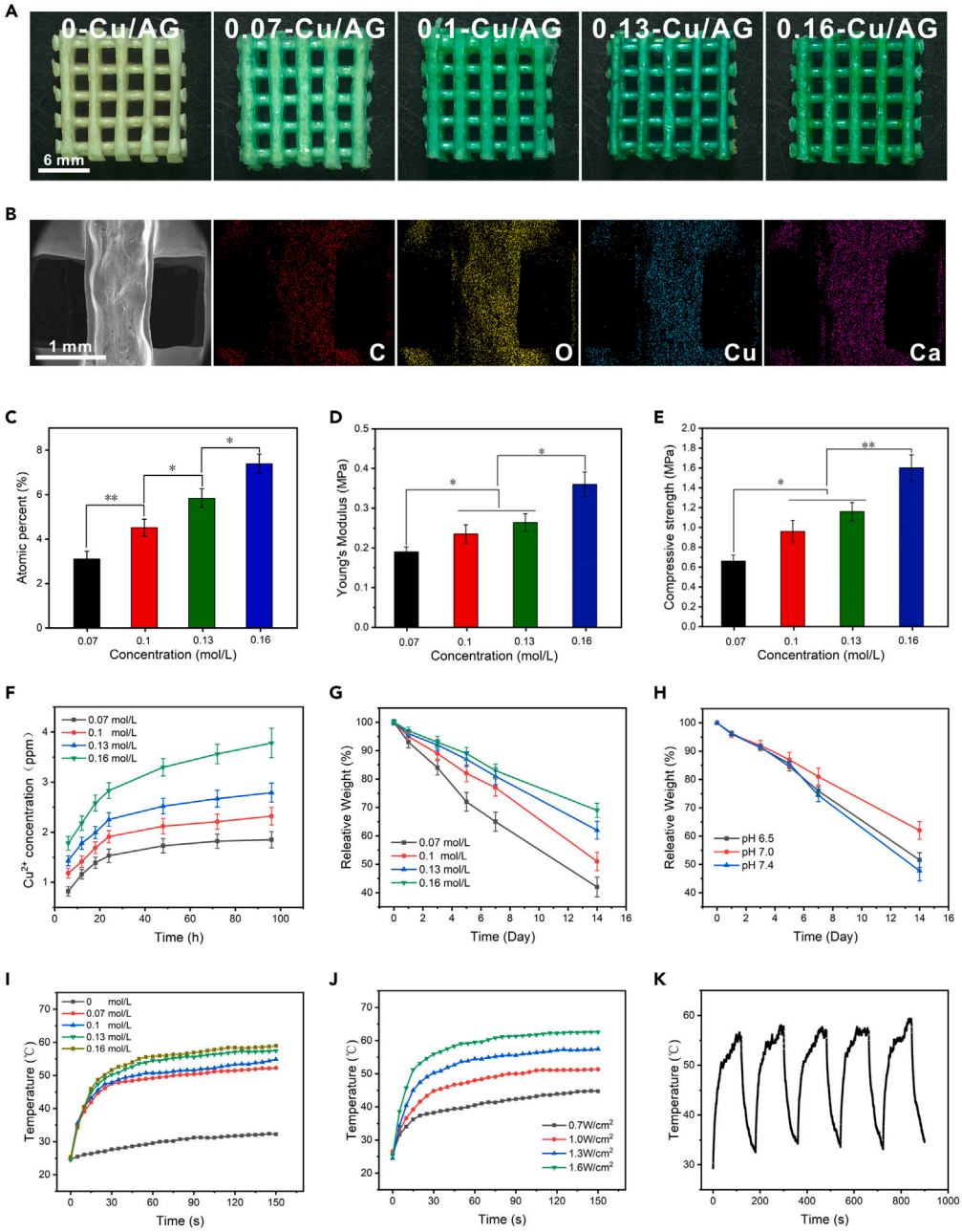


**Figure 1. Fabrication and characterization of Cu/AG scaffolds**

(A) Optical images of the Cu/AG scaffolds crosslinked with 0, 0.07, 0.1, 0.13, and 0.16 mol/L $CuCl_2$, respectively. Scale bar, 6 mm.

(B) Energy-dispersive X-ray spectroscopy (EDS) elemental mapping analysis of the 0.13-Cu/AG scaffold. Scale bar, 1 mm. See also Figure S2.

(C) Atomic percentage on the surface of Cu/AG scaffolds with different concentration of the crosslinking agent. Data are represented as mean ± SD. *$p < 0.05$, **$p < 0.01$.

(D) The Young's modulus of the Cu/AG scaffolds with different concentration of the crosslinking agent. *$p < 0.05$.

(E) The compressive strength of the Cu/AG scaffolds with different concentration of the crosslinking agent. *$p < 0.05$, **$p < 0.01$.

(F) *In vitro* release of copper ions from Cu/AG scaffolds with different concentration of the crosslinking agent.

(G) *In vitro* degradation of Cu/AG scaffolds with different concentration of the crosslinking agent.

(H) *In vitro* degradation of 0.13-Cu/AG scaffolds with different pH values.

(I) Photothermal heating curves of different Cu/AG scaffolds under NIR laser irradiation (1.3 $W/cm^2$).

(J) Photothermal heating curves of the 0.13-Cu/AG scaffolds under NIR laser irradiation at different laser power (0.7, 1.0, 1.3, and 1.6 $W/cm^2$). See also Figure S4.

(K) Photothermal stability of the 0.13-Cu/AG scaffolds under sequential laser on/off cycles. See also Figure S5.

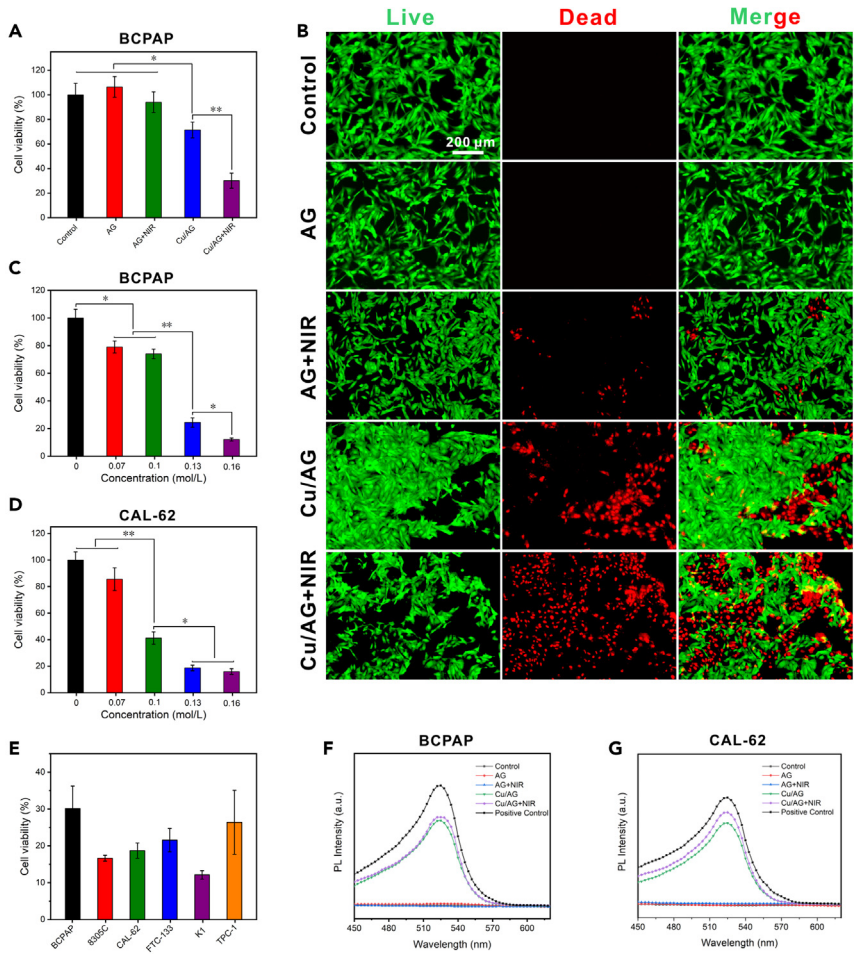


**Figure 2. Treatment of thyroid cancer cells with fiber scaffolds**

(A) Cell viability of BCPAP cells in different treatment groups. Data are represented as mean ± SD. *p < 0.05, **p < 0.01.

(B) Live and dead staining of BCPAP cells in different treatment groups. The concentration of $Cu^{2+}$ is 0.13 mol/L. Scale bar, 200 μm.

(C) Cell viability of BCPAP cells in the Cu/AG + NIR group with different capacities loaded of $Cu^{2+}$. *p < 0.05, **p < 0.01. See also Figure S6.

(D) Cell viability of CAL-62 cells in the Cu/AG + NIR group with different capacities loaded of $Cu^{2+}$. *p < 0.05, **p < 0.01. See also Figure S6.

(E) Cell viability of six thyroid cancer cell lines after treatment with 0.13-Cu/AG + NIR.

(F) The fluorescence intensity change curves of ROS production in BCPAP cells of different treatment groups.

(G) The fluorescence intensity change curves of ROS production in CAL-62 cells of different treatment groups.

where $h$ is the heat transfer coefficient, $A$ is the surface area of the container, $\Delta T_{max}$ is the temperature change of the 0.13-Cu/AG scaffold at the maximum steady-state temperature, $Q_s$ is the heat associated with the light absorbed by solvent, $I$ is the laser power, and $A_\lambda$ is the absorbance of the 0.13-Cu/AG scaffold at the wavelength of 808 nm. According to the equation, the $\eta$ value of 0.13-Cu/AG scaffold was calculated to be about 36.51%. The high photothermal conversion efficiency of the Cu/AG scaffold makes it a promising agent for PTT.

## Treatment of thyroid cancer cells using fiber scaffolds

Six thyroid cancer cell lines, BCPAP, 8305C, CAL-62, FTC-133, K1, and TPC-1, were used to evaluate the therapeutic effect of the Cu/AG stent on thyroid cancer. Cell viability of BCPAP cells in the 0.13-Cu/AG + NIR scaffold group decreased by 69.88%, while the 0.13-Cu/AG scaffold group showed a limited decrease of 29.7% (Figure 2A). Cell viability in the AG + NIR group remained over 94%. In contrast, AG scaffold has no significant effect on cell growth, indicating that the AG scaffold has non-cytotoxicity (Figure 2A). Live/dead staining of BCPAP cells in different treatment groups showed that the 0.13-Cu/AG + NIR (1.3 W/cm$^2$) scaffold induced significant and extensive cell death compared with other groups (Figure 2B). Subsequently, concentration gradient of $Cu^{2+}$ experiments was performed on the six thyroid cancer cell lines. Under NIR laser irradiation (1.3 W/cm$^2$), the 0.13-Cu/AG and 0.16-Cu/AG scaffolds triggered >70% cell ablation, which were far superior to the other groups (Figures 2C, 2D, and S6). Furthermore, cell viability measurements after treating the six thyroid cancer cell lines with 0.13-Cu/AG + NIR revealed that the 3D-printed copper-loaded scaffold had a broad-spectrum therapeutic effect on thyroid cancer cells (Figure 2E).

CDT is a promising approach for cancer treatment, which utilizes Fenton or Fenton-like reactions to generate toxic hydroxyl radicals, disrupt cellular redox homeostasis, and induce cell death. Several studies have shown that $Cu^{2+}$ can increase intracellular levels of ROS through Fenton-like reactions, leading to cell damage or death.[9–11] In this study, we examined the production of ROS in different treated groups. As shown in Figures 2F and 2G, the Cu/AG scaffold group exhibited the generation of ROS in BCPAP and CAL-62 cells, while the control, AG, and AG + NIR groups showed no ROS production. Additionally, the Cu/AG + NIR scaffold also induced ROS production, indicating that PDT induced by NIR may also be involved.

Collectively, these experiments suggest that the combination of CDT ($Cu^{2+}$) and PTT (heat) exhibits a synergistic effect on thyroid cancer cell lines, probably due to the enhanced cytotoxicity of $Cu^{2+}$ in the elevated temperature of the Cu/AG stent.

## Establishment and histological characterization of thyroid cancer organoid models

In the last decade, patient-derived organoids have facilitated basic cancer research and played an important role in personalized medicine. By developing organoids from human tumor tissues, they have opened new avenues for studying and treating various cancers. Tumor organoids have been utilized for generating biobanks, performing drug screening, and studying mutational signatures. In contrast to immortalized cancer cell lines that often cannot fully preserve intratumor heterogeneity and cellular diversity,[23,24] tumor organoids have been used as *ex vivo* models that faithfully recapitulate histological features, genetic alterations, and tumor heterogeneity of the original tumors. Animal models, particularly patient-derived mouse xenografts (PDXs), have provided significant insights into the cellular and genetic basis of tumors.[25] However, they are often costly, inefficient, time-consuming, and difficult to translate into clinical treatment.[26,27] Organoids have been used to model various types of cancer and can accurately predict patient responses to drugs and radiotherapy in the clinic.

In our study, six thyroid cancer organoid models were successfully established from surgically removed thyroid tumors (Figure 3A). The histological features of thyroid cancer organoids were compared with those of the parental tumors using H&E staining. Thyroid cancer organoids exhibited similar histological characteristics to those of the original tumors, including growth patterns and cellular and nuclear atypia (Figure 3B). Next, we assessed the expression of a panel of thyroid cancer biomarkers, cytokeratin 19 (CK19), galectin-3, and Ki-67, in tumor tissue-organoid pairs. Immunofluorescence staining demonstrated that the marker expression profile of each thyroid cancer organoid line matched that of its corresponding parental tumor (Figure 4). These results suggest that the histological characteristics and marker expression of the original tumors were well preserved in the derived organoid models.

## Treatment of thyroid cancer organoids using fiber scaffolds

To further confirm the therapeutic effect of the Cu/AG scaffolds on thyroid cancer, we used them to treat thyroid cancer organoids derived from six patients under NIR light. For instance, organoid viability of patient 1 in the 0.13-Cu/AG and 0.13-Cu/AG + NIR (1.3 $W/cm^2$) scaffold groups decreased by 68.7% and 95%, respectively (Figure 5A). Light microscopy imaging of thyroid cancer organoids derived from patient 1 and 3 showed that treatment of organoids with 0.13-Cu/AG + NIR resulted in an altered phenotypic appearance of organoids (Figure 5B). Furthermore, calcein-AM/PI staining indicated that Cu/AG+NIR-treated organoids from patient 1 (Figure 5C) and patient 3 (Figure 5D) exhibited significant and extensive cell death compared to the control group. The combination of CDT and PTT of Cu/AG stent showed a great therapeutic effect on thyroid cancer organoids derived from different patients, indicating a broad-spectrum antitumor effect in patients with thyroid cancer (Figure 5E).

The Cu/AG scaffold with NIR that we developed provides a promising therapeutic platform for localized treatment of thyroid cancer. $Cu^{2+}$ can simultaneously serve as a photothermal agent to mediate PTT and as a catalyst in Fenton-like reactions to generate ROS. On this platform, minimizing negative effects can be achieved by controlling the local concentration of $Cu^{2+}$ and the power of NIR. The combination of dual therapies can reduce the use of $Cu^{2+}$ and mitigate potential side effects. Our previous study has shown that low dose of $Cu^{2+}$ crosslinked scaffolds not only have minimal adverse effects on normal tissues but also promote tissue repair to some extent.[28] Furthermore, using low-density laser irradiation and shortening the irradiation time can significantly reduce side effects on normal cells and tissues. In this study, the Cu/AG scaffolds were manufactured through 3D printing, enabling customized shaping and structural design according to individual patient needs. The scaffolds can be implanted into the lesion site after surgery to prevent postoperative recurrence. The scaffold material exhibits high biocompatibility and rapid degradation rate and eliminates the secondary surgical removal after implantation.

## Conclusions

In this study, the functional Cu/AG hydrogel scaffolds with chemo-photothermal effect were prepared by 3D printing technology. The $Cu^{2+}$-loaded hydrogel scaffolds exhibited *in vitro* release dynamics and demonstrated excellent photothermal effect under NIR irradiation. The combination of copper ions and NIR therapy effectively killed thyroid cancer cells as well as thyroid cancer organoids derived from clinical samples. Notably, $Cu^{2+}$-based PTT and CDT combined treatment strategy not only avoids the limitations of single mode of cancer treatment but also optimizes the treatment effectiveness. Therefore, we believe that the 3D-printed hydrogel stent loaded with copper ions may be a potential candidate for local cancer treatment.

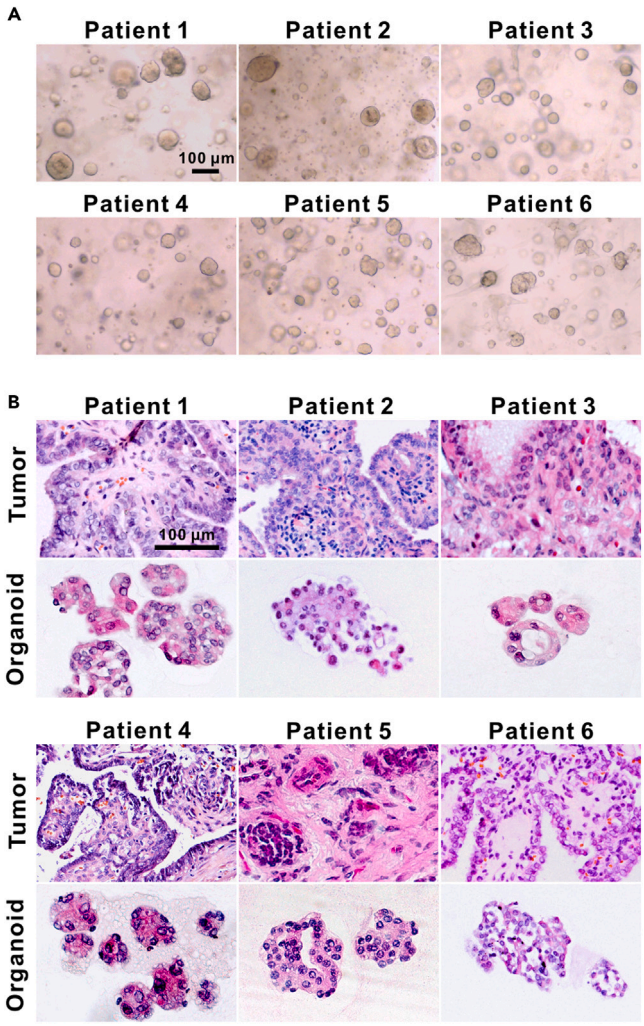


**Figure 3. Establishment and histological characteristics of thyroid cancer organoids**

(A) Representative bright-field microscopy images of thyroid cancer organoid lines. The passage number for each patient's organoid line was: patient 1, P3; patient 2, P2; patient 3, P4; patient 4, P5; patient 5, P4; patient 6, P3. Scale bar, 100 μm.

(B) H&E staining of thyroid cancer tissues and the derived organoids. Scale bar, 100 μm.

## Limitations of the study

In this paper, we demonstrated the significant inhibitory effect of the 3D-printed scaffold on the thyroid cancer cell lines and patient-derived organoids. The ongoing study to develop PDX models using thyroid cancer organoids will be more helpful in studying the therapeutic effects of 3D bioprinting scaffolds in *in vivo* experiments.

In addition to the PTT of the $Cu^{2+}$-loaded hydrogel scaffold combined with NIR, PDT induced by NIR may also be involved. However, the underlying mechanisms are still not well understood and require further study.

## STAR★METHODS

Detailed methods are provided in the online version of this paper and include the following:

- KEY RESOURCES TABLE
- RESOURCE AVAILABILITY
  - Lead contact
  - Materials availability
  - Data and code availability
- EXPERIMENTAL MODEL AND STUDY PARTICIPANT DETAILS

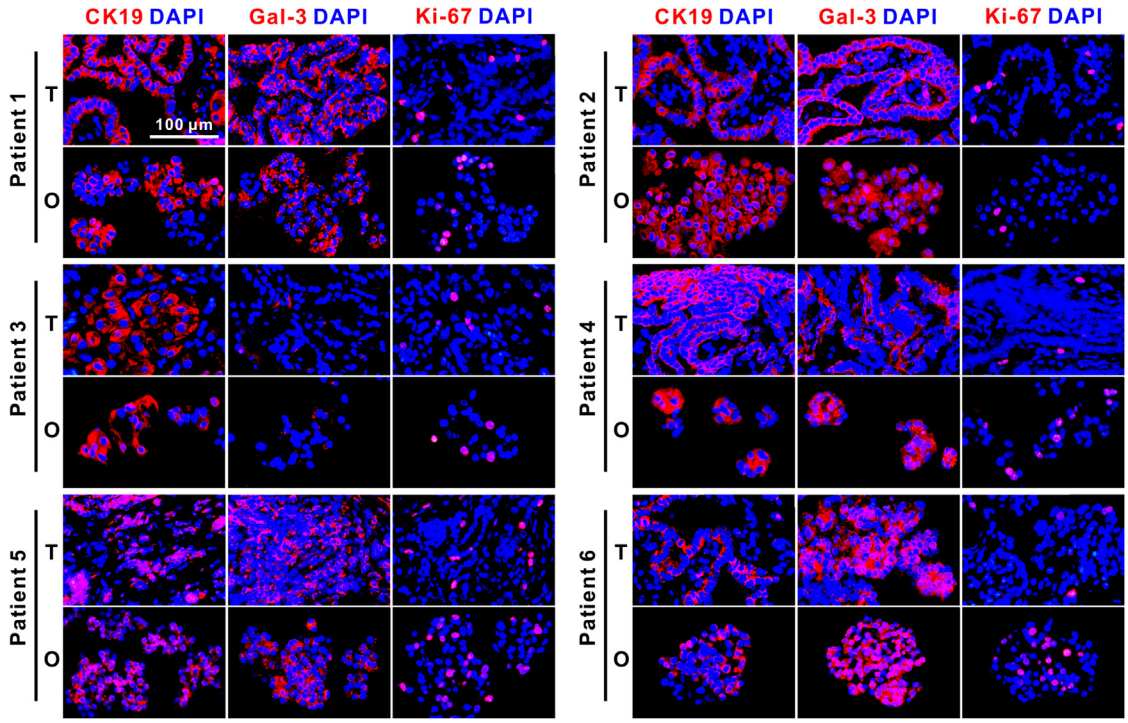


**Figure 4. Immunofluorescence staining of CK19, gal-3, and Ki-67 in the primary tumor tissues and the paired organoids**

The passage number for each patient's organoid line was: patient 1, P3; patient 2, P2; patient 3, P4; patient 4, P5; patient 5, P4; patient 6, P3. T, tumor; O, organoids; gal-3, galectin-3. Scale bar, 100 μm.



## SUPPLEMENTAL INFORMATION

Supplemental information can be found online at https://doi.org/10.1016/j.isci.2023.108076.

## ACKNOWLEDGMENTS

This work was supported by the National Key R&D Program of China (2019YFA0906000), the Guangdong Basic and Applied Basic Research Foundation (2021A1515110618, 2022A1515011428), the Shenzhen Science and Technology Program (KCXFZ20211020163407011, JCYJ20210324105612034), the Scientific Research Foundation of PEKING UNIVERSITY SHENZHEN HOSPITAL (KYQD2023251), the Shenzhen San-Ming Project (SZSM201612010), and the Guangdong Medical Science and Technology Research Foundation (B2022101).

## AUTHOR CONTRIBUTIONS

H.W., D.C., H.C., Y.L., and Y.Z. conceived the study and designed experiments; B.H., P.L., H.J., L.Z., H.Y., D.L., and W.W. recruited patients, performed operations, and collected and curated clinical annotation data; H.W., D.C., and H.Y. performed the experiments; all authors were

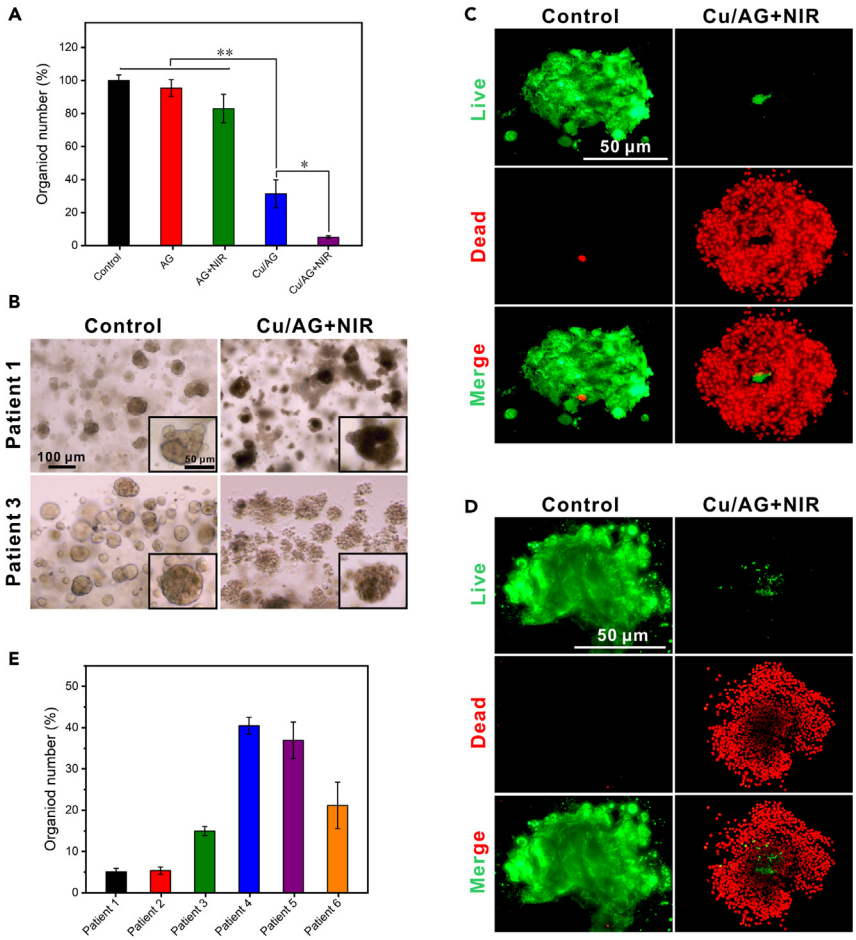


**Figure 5. Treatment of thyroid cancer organoids with fiber scaffolds**

(A) Cell viability of thyroid cancer organoids derived from patient 1 in different treatment groups. The concentration of $Cu^{2+}$ is 0.13 mol/L. Data are represented as mean ± SD. *$p < 0.05$, **$p < 0.01$.

(B) Representative bright-field images of thyroid cancer organoids in the control and 0.13-Cu/AG+NIR groups. Scale bar = 100 μm except the insets were 50 μm.

(C) Live and dead staining of thyroid cancer organoids derived from patient 1 in the control and 0.13-Cu/AG+NIR groups. Scale bar, 50 μm.

(D) Live and dead staining of thyroid cancer organoids derived from patient 3 in the control and 0.13-Cu/AG+NIR groups. Scale bar, 50 μm.

(E) Cell viability of thyroid cancer organoid lines derived from six patients after treatment with 0.13-Cu/AG + NIR.

involved in data analysis and interpretation of the results; H.W., D.C., Y.L., and Y.Z. wrote the manuscript. All authors reviewed and gave final approval.

## DECLARATION OF INTERESTS

The authors declare no competing interests.

## INCLUSION AND DIVERSITY

We support inclusive, diverse, and equitable conduct of research.

Received: June 15, 2023
Revised: August 10, 2023
Accepted: September 25, 2023
Published: September 27, 2023

## REFERENCES


1. Huang, X., Lu, Y., Guo, M., Du, S., and Han, N. (2021). Recent strategies for nano-based PTT combined with immunotherapy: from a biomaterial point of view. Theranostics *11*, 7546–7569. https://doi.org/10.7150/thno.56482.
2. Ahmad, R., Fu, J., He, N., and Li, S. (2016). Advanced Gold Nanomaterials for Photothermal Therapy of Cancer. J. Nanosci. Nanotechnol. *16*, 67–80. https://doi.org/10.1166/jnn.2016.10770.
3. Nam, J., Son, S., Ochyl, L.J., Kuai, R., Schwendeman, A., and Moon, J.J. (2018). Chemo-photothermal therapy combination elicits anti-tumor immunity against advanced metastatic cancer. Nat. Commun. *9*, 1074. https://doi.org/10.1038/s41467-018-03473-9.
4. Yata, T., Takahashi, Y., Tan, M., Nakatsuji, H., Ohtsuki, S., Murakami, T., Imahori, H., Umeki, Y., Shiomi, T., Takakura, Y., and Nishikawa, M. (2017). DNA nanotechnology-based composite-type gold nanoparticle-immunostimulatory DNA hydrogel for tumor photothermal immunotherapy. Biomaterials *146*, 136–145. https://doi.org/10.1016/j.biomaterials.2017.09.014.
5. Cao, C., Wang, X., Yang, N., Song, X., and Dong, X. (2022). Recent advances of cancer chemodynamic therapy based on Fenton/Fenton-like chemistry. Chem. Sci. *13*, 863–889. https://doi.org/10.1039/d1sc05482a.
6. Zhang, C., Bu, W., Ni, D., Zhang, S., Li, Q., Yao, Z., Zhang, J., Yao, H., Wang, Z., and Shi, J. (2016). Synthesis of Iron Nanometallic Glasses and Their Application in Cancer Therapy by a Localized Fenton Reaction. Angew. Chem., Int. Ed. Engl. *55*, 2101–2106. https://doi.org/10.1002/anie.201510031.
7. Zhao, Y., Chen, B.Q., Kankala, R.K., Wang, S.B., and Chen, A.Z. (2020). Recent Advances in Combination of Copper Chalcogenide-Based Photothermal and Reactive Oxygen Species-Related Therapies. ACS Biomater. Sci. Eng. *6*, 4799–4815. https://doi.org/10.1021/acsbiomaterials.0c00830.
8. Hessel, C.M., Pattani, V.P., Rasch, M., Panthani, M.G., Koo, B., Tunnell, J.W., and Korgel, B.A. (2011). Copper selenide nanocrystals for photothermal therapy. Nano Lett. *11*, 2560–2566. https://doi.org/10.1021/nl201400z.
9. Lu, J., Jiang, Z., Ren, J., Zhang, W., Li, P., Chen, Z., Zhang, W., Wang, H., and Tang, B. (2022). One-Pot Synthesis of Multifunctional Carbon-Based Nanoparticle-Supported Dispersed Cu2+ Disrupts Redox Homeostasis to Enhance CDT. Angew. Chem., Int. Ed. Engl. *61*, e202114373. https://doi.org/10.1002/anie.202114373.
10. Ma, B., Wang, S., Liu, F., Zhang, S., Duan, J., Li, Z., Kong, Y., Sang, Y., Liu, H., Bu, W., and Li, L. (2019). Self-Assembled Copper-Amino Acid Nanoparticles for in Situ Glutathione "AND" H2O2 Sequentially Triggered Chemodynamic Therapy. J. Am. Chem. Soc. *141*, 849–857. https://doi.org/10.1021/jacs.8b08714.
11. Poyton, M.F., Sendecki, A.M., Cong, X., and Cremer, P.S. (2016). Cu(2+) Binds to Phosphatidylethanolamine and Increases Oxidation in Lipid Membranes. J. Am. Chem. Soc. *138*, 1584–1590. https://doi.org/10.1021/jacs.5b11561.
12. Tian, Q., Tang, M., Sun, Y., Zou, R., Chen, Z., Zhu, M., Yang, S., Wang, J., Wang, J., and Hu, J. (2011). Hydrophilic flower-like CuS superstructures as an efficient 980 nm laser-driven photothermal agent for ablation of cancer cells. Adv. Mater. *23*, 3542–3547. https://doi.org/10.1002/adma.201101295.
13. Zhou, M., Zhang, R., Huang, M., Lu, W., Song, S., Melancon, M.P., Tian, M., Liang, D., and Li, C. (2010). A chelator-free multifunctional [64Cu]CuS nanoparticle platform for simultaneous micro-PET/CT imaging and photothermal ablation therapy. J. Am. Chem. Soc. *132*, 15351–15358. https://doi.org/10.1021/ja106855m.
14. Luo, B., Chen, L., Hong, Z., You, X., Huang, F.P., Bian, H.D., Zhang, L., and Zhao, S. (2021). A simple and feasible atom-precise biotinylated Cu(i) complex for tumor-targeted chemodynamic therapy. Chem. Commun. *57*, 6046–6049. https://doi.org/10.1039/d1cc00515d.
15. Du, W., Zong, Q., Guo, R., Ling, G., and Zhang, P. (2021). Injectable Nanocomposite Hydrogels for Cancer Therapy. Macromol. Biosci. *21*, e2100186. https://doi.org/10.1002/mabi.202100186.
16. Kwon, I.K., Lee, S.C., Han, B., and Park, K. (2012). Analysis on the current status of targeted drug delivery to tumors. J. Control Release *164*, 108–114. https://doi.org/10.1016/j.jconrel.2012.07.010.
17. Lee, K.Y., and Mooney, D.J. (2012). Alginate: properties and biomedical applications. Prog. Polym. Sci. *37*, 106–126. https://doi.org/10.1016/j.progpolymsci.2011.06.003.
18. Cheng, N.C., Lin, W.J., Ling, T.Y., and Young, T.H. (2017). Sustained release of adipose-derived stem cells by thermosensitive chitosan/gelatin hydrogel for therapeutic angiogenesis. Acta Biomater. *51*, 258–267. https://doi.org/10.1016/j.actbio.2017.01.060.
19. Yang, G., Lin, H., Rothrauff, B.B., Yu, S., and Tuan, R.S. (2016). Multilayered polycaprolactone/gelatin fiber-hydrogel composite for tendon tissue engineering. Acta Biomater. *35*, 68–76. https://doi.org/10.1016/j.actbio.2016.03.004.
20. Dong, C., Wei, H., Zhang, X., Li, Y., Huang, L., Wa, Q., and Luo, Y. (2022). 3D printed hydrogel/wesselsite-PCL composite scaffold with structural change from core/shell fibers to microchannels for enhanced bone regeneration. Compos. B Eng. *246*, 110264. https://doi.org/10.1016/j.compositesb.2022.110264.
21. Wei, X., Liu, C., Wang, Z., and Luo, Y. (2020). 3D printed core-shell hydrogel fiber scaffolds with NIR-triggered drug release for localized therapy of breast cancer. Int. J. Pharm. *580*, 119219. https://doi.org/10.1016/j.ijpharm.2020.119219.
22. Zhang, X., Wei, H., Dong, C., Wang, J., Zhang, T., Huang, L., Ni, D., and Luo, Y. (2023). 3D printed hydrogel/bioceramics core/shell scaffold with NIR-II triggered drug release for chemo-photothermal therapy of bone tumors and enhanced bone repair. Chem. Eng. J. *461*, 141855. https://doi.org/10.1016/j.cej.2023.141855.
23. Domcke, S., Sinha, R., Levine, D.A., Sander, C., and Schultz, N. (2013). Evaluating cell lines as tumour models by comparison of genomic profiles. Nat. Commun. *4*, 2126. https://doi.org/10.1038/ncomms3126.
24. Sachs, N., and Clevers, H. (2014). Organoid cultures for the analysis of cancer phenotypes. Curr. Opin. Genet. Dev. *24*, 68–73. https://doi.org/10.1016/j.gde.2013.11.012.
25. Cheon, D.J., and Orsulic, S. (2011). Mouse models of cancer. Annu. Rev. Pathol. *6*, 95–119. https://doi.org/10.1146/annurev.pathol.3.121806.154244.
26. Drost, J., and Clevers, H. (2018). Organoids in cancer research. Nat. Rev. Cancer *18*, 407–418. https://doi.org/10.1038/s41568-018-0007-6.
27. Tuveson, D., and Clevers, H. (2019). Cancer modeling meets human organoid technology. Science *364*, 952–955. https://doi.org/10.1126/science.aaw6985.
28. Luo, Y., Zhang, T., and Lin, X. (2022). 3D printed hydrogel scaffolds with macro pores and interconnected microchannel networks for tissue engineering vascularization. Chem. Eng. J. *430*, 132926. https://doi.org/10.1016/j.cej.2021.132926.
29. Liu, Y., Ai, K., Liu, J., Deng, M., He, Y., and Lu, L. (2013). Dopamine-melanin colloidal nanospheres: an efficient near-infrared photothermal therapeutic agent for in vivo cancer therapy. Adv. Mater. *25*, 1353–1359. https://doi.org/10.1002/adma.201204683.
30. Ren, W., Yan, Y., Zeng, L., Shi, Z., Gong, A., Schaaf, P., Wang, D., Zhao, J., Zou, B., Yu, H., et al. (2015). A Near Infrared Light Triggered Hydrogenated Black TiO2 for Cancer Photothermal Therapy. Adv. Healthcare Mater. *4*, 1526–1536. https://doi.org/10.1002/adhm.201500273.
31. Roper, D.K., Ahn, W., and Hoepfner, M. (2007). Microscale Heat Transfer Transduced by Surface Plasmon Resonant Gold Nanoparticles. J. Phys. Chem. C Nanomater. Interfaces *111*, 3636–3641. https://doi.org/10.1021/jp064341w.
32. Zhou, J., Lu, Z., Zhu, X., Wang, X., Liao, Y., Ma, Z., and Li, F. (2013). NIR photothermal therapy using polyaniline nanoparticles. Biomaterials *34*, 9584–9592. https://doi.org/10.1016/j.biomaterials.2013.08.075.
33. Chen, D., Tan, Y., Li, Z., Li, W., Yu, L., Chen, W., Liu, Y., Liu, L., Guo, L., Huang, W., and Zhao, Y. (2021). Organoid Cultures Derived From Patients With Papillary Thyroid Cancer. J. Clin. Endocrinol. Metab. *106*, 1410–1426. https://doi.org/10.1210/clinem/dgab020.
34. Chen, D., Su, X., Zhu, L., Jia, H., Han, B., Chen, H., Liang, Q., Hu, C., Yang, H., Liu, L., et al. (2023). Papillary thyroid cancer organoids harboring BRAFV600E mutation reveal potentially beneficial effects of BRAF inhibitor-based combination therapies. J. Transl. Med. *21*, 9. https://doi.org/10.1186/s12967-022-03848-z.

## STAR★METHODS

### KEY RESOURCES TABLE

| REAGENT or RESOURCE | SOURCE | IDENTIFIER |
|---|---|---|
| Antibodies | | |
| Galectin-3 | Abcam | Cat#ab76245; Clone: EP2775Y; RRID: AB_2265782 |
| Ki-67 | Abcam | Cat#ab16667; Clone: SP6; RRID: AB_302459 |
| Cytokeratin 19 (CK19) | Affinity Biosciences | Cat#AF5106; RRID: AB_2837592 |
| Cy3-labeled goat anti-rabbit IgG (H + L) | Beyotime | Cat#A0516; RRID: AB_2893015 |
| Biological samples | | |
| Human papillary thyroid cancer tissues | This study | N/A |
| Chemicals, peptides, and recombinant proteins | | |
| B27 | Gibco | Cat#17504-044 |
| N-acetyl-L-cysteine | Sigma-Aldrich | Cat#A9165 |
| Nicotinamide | Sigma-Aldrich | Cat#N0636 |
| R-spondin-1 | Peprotech | Cat#120-38 |
| Noggin | Peprotech | Cat#120-10C |
| SB202190 | Sigma-Aldrich | Cat#S7067 |
| A83-01 | Sigma-Aldrich | Cat#SML0788 |
| EGF | Peprotech | Cat#AF-100-15 |
| FGF-7 | Peprotech | Cat#100-19 |
| FGF-10 | Peprotech | Cat#100-26 |
| Y-27632 dihydrochloride | Abmole | Cat#M1817 |
| Sodium alginate | Sigma-Aldrich | Cat#71238 |
| Gelatin | Sigma-Aldrich | Cat#73865 |
| Calcium chloride | Macklin | Cat#C805225 |
| Cupric chloride | Macklin | Cat#C805298 |
| Critical commercial assays | | |
| CellTiter-Glo 3D Reagent | Promega | Cat#G9683 |
| Cell Counting Kit-8 | MedChemExpress | Cat#HY-K0301 |
| Reactive Oxygen Species Assay Kit | Beyotime | Cat# S0033S |
| Calcein-AM | Biolegend | Cat#425201 |
| Propidium iodide | Biolegend | Cat#421301 |
| Experimental models: Cell lines | | |
| BCPAP | Shanghai Institute of Biochemistry and Cell Biology, Chinese Academy of Sciences, China | Cat#SCSP-543 |
| 8305C | Shanghai Institute of Biochemistry and Cell Biology, Chinese Academy of Sciences, China | Cat#SCSP-540 |
| CAL-62 | Shanghai Institute of Biochemistry and Cell Biology, Chinese Academy of Sciences, China | Cat#SCSP-546 |
| K1 | iCell Bioscience Inc., Shanghai, China | Cat#iCell-h394 |
| FTC-133 | Cobioer Biosciences Co., Ltd., Nanjing, China | Cat#CBP61109 |
| TPC-1 | Cobioer Biosciences Co., Ltd., Nanjing, China | Cat#CBP60257 |
| Experimental models: Organisms/strains | | |
| Human papillary thyroid cancer organoids | This study | N/A |

(*Continued on next page*)

*Continued*

| REAGENT or RESOURCE | SOURCE | IDENTIFIER |
|---|---|---|
| Software and algorithms | | |
| Prism GraphPad 7.0 | GraphPad Software, Inc., CA, USA | N/A |
| SPSS 19.0 | SPSS, Inc., IL, USA | N/A |
| OriginPro 8.0 | OriginLab Corporation, Northampton, MA, USA | N/A |
| CorelDraw X7 | Corel Corporation, Ottawa, Canada | N/A |

## RESOURCE AVAILABILITY

### Lead contact

Further information and requests for reagents and resources should be directed to and will be fulfilled by the lead contact, Prof. Yongsheng Zhao (zhaoys69@126.com).

### Materials availability

The study did not generate new unique reagents and there are no restrictions to availability.

### Data and code availability

- All data reported in this paper will be shared by the lead contact upon request.
- This paper does not report original code.
- Any additional information required to reanalyze the data reported in this paper is available from the lead contact upon request.

## EXPERIMENTAL MODEL AND STUDY PARTICIPANT DETAILS

### Cell lines

Human thyroid cancer cell lines BCPAP, 8305C, and CAL-62 with STR verification were obtained from Shanghai Institute of Biochemistry and Cell Biology, Chinese Academy of Sciences, China. Human thyroid cancer cell lines TPC-1 and FTC-133 with STR verification were purchased from Cobioer Biosciences Co., Ltd. (Nanjing, China), and K1 was purchased from iCell Bioscience Inc. (Shanghai, China). All cell lines were routinely cultured in RPMI 1640 or DMEM medium (VivaCell, Shanghai, China) supplemented with 10% fetal bovine serum (10099-141, Gibco), 1% sodium pyruvate (11360-070, Gibco) and 1% non-essential amino acids (11140-050, Gibco) at 37°C with 5% $CO_2$.

### Human subjects and sample collection

Human thyroid cancer tissues were obtained from six patients (four females, 15–43 years old; two males, 28 and 40 years old) at Peking University Shenzhen Hospital, Shenzhen, China. The detailed clinical information of patients is described in Table S1.

The study was approved by the Human Ethical Committee of Peking University Shenzhen Hospital (approval number: 2022-147). The design of this study is in accordance with the Declaration of Helsinki. All patients provided written informed consent before sample collection.

The resected tumor tissues were transferred to ice-cold adDMEM/F12$^{+++}$ medium [advanced DMEM/F12 medium (12634-010, Gibco) containing 10 mM HEPES (15630-080, Gibco), 1 × GlutaMAX (3505-0061, Gibco), and 1% antibiotic-antimycotic (15240-062, Gibco)] and shipped to the laboratory on ice for immediate further processing.

## METHOD DETAILS

### Materials

Gelatin from porcine skin and sodium alginate from brown algae were obtained from Sigma-Aldrich. Calcium chloride ($CaCl_2$) and cupric chloride ($CuCl_2$) were purchased from Macklin (Shanghai, China).

### Preparation and characterization of fiber scaffolds

The alginate/gelatin-based printing inks were prepared by mixing 2 g of alginate powder with 10 g of prepared 9 wt % gelatin solution. After the inks were thoroughly mixed, they were loaded into the printing tube equipped with an 18 G nozzle and a 3D printing system (Bioscaffolder 3.1 from Gesim, Germany) was used to produce the hydrogel scaffolds. The printing speed was set at 3.5 mm/s with a dosing pressure of 5–6 bar, and the temperature was kept at 60°C. After fabricating the scaffolds, crosslink the fiber scaffolds with $CuCl_2$ (0.07, 0.1, 0.13 and 0.16 mol/L) for 3 min, and then crosslink with 1 mol/L $CaCl_2$ for 1 min. The morphology of the prepared scaffolds was observed by a stereoscopic microscope (TOKYO 163–0914, Japan). The microstructure and elements of the scaffolds were characterized using scanning electron microscopy (SEM, FEI APREO S, Thermo Scientific, Netherland) and energy-dispersive X-ray spectroscopy (EDS). The photothermal performance of the scaffolds was evaluated by 808 nm NIR laser with different power densities (0.7–1.6 W/cm$^2$). The compressive strength of the

Cu/AG scaffold (8 × 8 × 6 mm) was measured by a universal testing machine (HZ1007C, LI XIAN YI QI, China) at a cross-head rate of 5 mm/min. The modulus was taken from the slope of the liner segment of the strain-stress curve.

### Photothermal conversion efficiency of Cu/AG scaffold

Photothermal conversion efficiency ($\eta$) of the 0.13-Cu/AG scaffold was calculated according to the methods reported previously.[29–32] The $\eta$ value can be calculated according to the following equation:

$$\eta = \frac{hA\Delta T_{max} - Qs}{I\left(1 - 10^{-A\lambda}\right)}$$

where $h$ is the heat transfer coefficient, $A$ is the surface area of the container, $\Delta T_{max}$ is the temperature change of the 0.13-Cu/AG scaffold at the maximum steady-state temperature, $Q_s$ is the heat associated with the light absorbed by solvent, $I$ is the laser power, and $A_\lambda$ is the absorbance of the 0.13-Cu/AG scaffold at the wavelength of 808 nm. Details of the calculation process are given as following:

The total energy balance of this system as following equation:

$$\sum_i m_i C_{p,i} \frac{dT}{dt} = Q_{Cu/AG} + Qs - Q_{loss} \quad \text{(Equation 1)}$$

where $m$ and $C_p$ are the mass and heat capacity, respectively. $T$ is the solution temperature. $Q_{Cu/AG}$ is the photothermal energy absorbed by the 0.13-Cu/AG scaffold:

$$Q_{Cu/AG} = I\left(1 - 10^{-A\lambda}\right)\eta \quad \text{(Equation 2)}$$

where $I$ is the laser power, $A_\lambda$ is the absorbance of the 0.13-Cu/AG scaffold at 808 nm, and $\eta$ is the photothermal conversion efficiency of the 0.13-Cu/AG scaffold. $Q_{loss}$ is thermal energy lost to the surroundings:

$$Q_{loss} = hA\Delta T \quad \text{(Equation 3)}$$

where $h$ is the heat transfer coefficient, $A$ is the surface area of the container, and $\Delta T$ is the temperature change, which is defined as $T$-$T_{surr}$ ($T$ and $T_{surr}$ are the solution temperature and ambient temperature of the surroundings, respectively). $Q_s$ is the heat associated with the light absorbed by solvent. At the maximum steady-state temperature, the heat input is equal to the heat output, so the equation can be:

$$Q_{Cu/AG} + Qs = Q_{loss} = hA\Delta T_{max} \quad \text{(Equation 4)}$$

where $\Delta T_{max}$ is the temperature change at the highest steady-state temperature. According to the Equations 2 and 4, $\eta$ can be determined:

$$\eta = \frac{hA\Delta T_{max} - Qs}{I\left(1 - 10^{-A\lambda}\right)} \quad \text{(Equation 5)}$$

In this equation, only $hA$ is unknown for calculation. In order to get $hA$, we herein introduce $\theta$, which is defined as the ratio of $\Delta T$ to $\Delta T_{max}$:

$$\theta = \frac{\Delta T}{\Delta T_{max}} \quad \text{(Equation 6)}$$

Substituting Equation 6 into Equation 1, and rearranging Equation 1:

$$\frac{d\theta}{dt} = \frac{hA}{\sum_i m_i C_{p,i}}\left[\frac{Q_{Cu/AG}+Qs}{hA\Delta T_{max}} - \theta\right] \quad \text{(Equation 7)}$$

When the laser was turned off, the $Q_{Cu/AG} + Q_s = 0$, so Equation 7 changed to:

Integrating Equation 8 gives the expression:

$$dt = -\frac{\sum_i m_i C_{p,i}}{hA}\frac{d\theta}{\theta} \quad \text{(Equation 8)}$$

$$t = -\frac{\sum_i m_i C_{p,i}}{hA}\theta \quad \text{(Equation 9)}$$

Thus, $hA$ can be determined by applying the linear time data from the cooling period vs. $-ln\theta$ (Figure S7). By substituting the $hA$ value into Equation 5, the photothermal conversion efficiency ($\eta$) of the 0.13-Cu/AG scaffold can be calculated.

### *In vitro* degradation and copper ion release

For *in vitro* degradation testing, incubate the scaffolds in PBS solution at 37°C. The ratio of PBS volume to scaffold mass was 20 mL/g, and PBS was refreshed daily. Among them, the 0.13-Cu/AG scaffold was selected for degradation testing in PBS solutions with different pH values (6.5, 7.0, and 7.4). Then calculate the relative weight of the scaffolds. The remaining solution was collected to measure copper ion release using an Avio 200 ICP-OES System (PerkinElmer Inc., USA).

### Organoid culture

Thyroid cancer organoids were generated following procedures previously reported by our group.[33,34] Briefly, collagenase digestion was used to isolate cells and small cell clusters from thyroid cancer samples. Mechanical digestion with a plastic pasteur pipette (320411, SORFA Life Science, China) was performed every 10 min during incubation. The mixture was then filtered using a 70-μm nylon mesh (258368, NEST Biotechnology, China), and embedded in Matrigel (356231, Corning). Thyroid cancer organoids were cultured in a basic growth medium consisting adDMEM/F12$^{+++}$ medium, 1 × B27 (17504-044, Gibco), 500 ng/mL of R-spondin-1 (120-38, Peprotech), 50 ng/mL of EGF (AF-100-15, Peprotech), 100 ng/mL of Noggin (120-10C, Peprotech), and 10 μM of SB202190 (S7067, Sigma-Aldrich) as the main components. Additionally, 10 μM of Y-27632 dihydrochloride (M1817, Abmole, USA) was added to the growth medium during the first 2 weeks of culture. The medium was refreshed every 3 days, and organoids were passaged at a ratio of 1:2-1:3 about every 2 weeks.

### Histology

Primary tumor tissues and the derived organoids were fixed in 10% formalin at 4°C for 24 h, followed by dehydration, paraffin-embedding, and serial sectioning at a thickness of 4-μm. Histological analysis of all the tumor and organoid samples was performed by a board-certified pathologist. Histopathological diagnosis was made according to the standard classification system.

### Immunofluorescence staining

Tissue and organoid slides were subjected to immunofluorescence analysis using standard procedures. The sections were incubated with primary antibodies against cytokeratin 19 (CK19; 1:200 dilution, AF5106, Affinity Biosciences), galectin-3 (1:300 dilution, ab76245, Abcam), and Ki-67 (1:300 dilution, ab16667, Abcam) at 4°C overnight. The sections were subsequently incubated with the secondary antibody Cy3-labeled goat anti-rabbit IgG (H + L) (1:300 dilution, A0516, Beyotime, China) for 1 h in the dark at room temperature. Nuclei were counterstained with DAPI for 10 min. Images were captured with a Carl Zeiss immunofluorescent microscope.

### Treatment of cell lines and organoids with fiber scaffolds

Thyroid cancer cells were seeded into 24-well plates at a density of 1 × $10^4$ cells per well and cultured at for 24 h. The scaffolds loaded with different concentrations of copper ions were coculture with cells for 24 h. Scaffolds were further exposed to NIR laser irradiation at 1.3 W/cm$^2$ for 2.5 min. After incubation for another 12 h, the cell viability was measured by Cell Counting Kit-8 (CCK-8; HY-K0301, MedChemExpress, USA) cell cytotoxicity assay. According to the experimental results, scaffold with 0.13 mol/L copper ions was selected for the next experiment.

The scaffolds were added to cell culture plates and divided into six treatment groups: (1) $Cu^{2+}$-loaded hydrogel scaffold with irradiation (Cu/AG + NIR); (2) $Cu^{2+}$-loaded hydrogel scaffold without irradiation (Cu/AG); (3) hydrogel scaffold with irradiation (AG + NIR); (4) hydrogel scaffold without irradiation (AG); (5) without any treatment (Control).

Thyroid cancer organoids were resuspended in 75% matrigel/growth medium (1,000 organoids per drop) and plated in triplicate in 24-well plates. On the third day, the scaffold loaded with 0.13 mol/L copper ions was cocultured with organoids. The treatment method is the same as described above for the cell experiments. The viability of organoids was assessed using CellTiter-Glo 3D Reagent (G9683, Promega) in accordance with the manufacturer's instructions, and luminescence readings were measured using a microplate reader (BioTek, USA).

For live and dead cell staining, cells or organoids were double-stained in the dark with 5 μM of calcein-AM (425201, Biolegend, USA) and 5 μM of propidium iodide (PI) (421301, Biolegend) for 20 min. Then, the cells or organoids were washed twice with PBS, and observed with a Carl Zeiss immunofluorescent microscope.

The level of intracellular ROS in BCPAP and CAL-62 cells was measured with a ROS Assay Kit (S0033S, Beyotime, China) according to the manufacture' instructions. 2',7'-dichlorodihydrofluorescin diacetate (DCFH-DA) was used to detect the ROS generation effect of the Cu/AG scaffolds. The fluorescence intensity in each well was detected by a fluorescence microplate reader and expressed as arbitrary units.

## QUANTIFICATION AND STATISTICAL ANALYSIS

All data were obtained from at least three independent experiments, and results were expressed as mean ± standard deviation (SD) using one-way ANOVA analysis. Differences were considered statistically significant at *$p < 0.05$ and **$p < 0.01$.